Feasibility study of beam-expanding telescopes in the interferometer arms for the Einstein Telescope

Samuel Rowlinson,[1] Artemiy Dmitriev,[1] Aaron W. Jones,[2] Teng Zhang,[1] and Andreas Freise[1,3,4]

[1]*School of Physics and Astronomy, and Institute of Gravitational Wave Astronomy, University of Birmingham, Edgbaston, Birmingham B15 2TT, United Kingdom*
[2]*OzGrav, University of Western Australia, Perth WA 6009, Crawley, Western Australia, Australia*
[3]*Department of Physics and Astronomy, VU Amsterdam, De Boelelaan 1081, 1081 HV, Amsterdam, Netherlands*
[4]*Nikhef, Science Park 105, 1098 XG Amsterdam, Netherlands*

(Received 6 November 2020; accepted 15 December 2020; published 5 January 2021)

The optical design of the Einstein Telescope (ET) is based on a dual-recycled Michelson interferometer with Fabry-Perot cavities in the arms. ET will be constructed in a new infrastructure, allowing us to consider different technical implementations beyond the constraints of the current facilities. In this paper we investigate the feasibility of using beam-expander telescopes in the interferometer arms. We provide an example implementation that matches the optical layout as presented in the ET design update 2020. We further show that the beam-expander telescopes can be tuned to compensate for mode mismatches between the arm cavities and the rest of the interferometer.

DOI: 10.1103/PhysRevD.103.023004

I. INTRODUCTION

The Einstein Telescope (ET) is a proposed *third-generation* gravitational-wave detector [1]. Once constructed, ET will provide an unprecedented level of sensitivity enabling: precise tests of general relativity, studies of compact binary coalesces involving both intermediate black holes and neutron stars, and will be sensitive enough to test several dark matter candidates [2]. ET combines a unique layout and design combining well-proven concepts from current gravitational-wave detectors with new technology. Figure 1 shows a sketch with the basic features of the layout: the ET observatory is composed of three detectors that together form an equilateral triangle. Each detector consists of two interferometers, one low-frequency detector (ET-LF) with its sensitivity optimised for low frequencies from 3 to 30 Hz and another high-frequency detector (ET-HF) with its sensitivity optimized for high frequencies from 30 Hz to 10 kHz. Similarly to current generation gravitational-wave detectors, i.e., Advanced LIGO [3] and Advanced Virgo [4], each interferometer in ET is a Fabry-Perot Michelson interferometer with power and signal recycling cavities (PRC and SRC, respectively) for arm cavity power enhancement and shaping the signal response [5], respectively. This interferometer configuration presented in [1] represents the initial detector anticipated to be installed, with upgrades and refinements to be implemented over several decades. The details of the design of the initial detector will be prepared, in sync with research and development of the required technology, over the next years.

The Fabry-Perot cavities in the arms of the detectors are designed to have large beam sizes on the test mass mirrors, i.e., the input test mass (ITM) and end test mass (ETM), for reducing the impact of thermal noise of the optics on the detector sensitivity. Beam-expander telescopes are used to match input light with smaller beam diameters to the larger beams in the arm cavities. In Advanced LIGO such telescopes are located between the beam splitter and the recycling mirrors [6], and in Advanced Virgo similar telescopes are part of the input-output optics outside the main interferometer [7]. However, in the ET the beam sizes on the main mirrors are significantly larger, requiring a very large substrate for the central beam splitter, larger than the main optics, due to the angle of incidence of 60°. In this paper we investigate the feasibility of an alternative layout with beam-expander telescopes located between the main beam splitter (BS) and the arm cavities. Such telescopes would provide smaller beam sizes in the central interferometer formed by the beam splitter, power recycling mirror (PRM) and signal recycling mirror (SRM), allowing for using much smaller optical components. This not only reduces the cost and complexity of these optics and their suspension systems, but also simplifies the mitigation of secondary reflections and scattered light, and reduces the effect of beam jitter [8]. Figure 2 shows a sketch of the optical layout in the lower left corner of the ET triangle, including possible locations for the beam expansion telescopes. An additional advantage of positioning the telescopes between the beam splitter and arm cavity is that Z-shaped telescopes provide flexibility in beam steering;

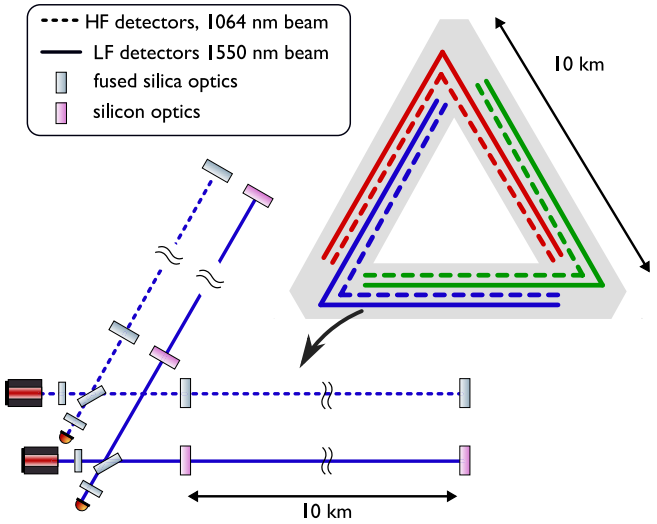

FIG. 1. The diagram on the top left shows a general overview of the ET observatory layout, with three detectors forming a equilateral triangle of 10 km length. Bottom left is a sketch that shows that each detector consists of two interferometers, one optimized for high frequencies (HF) and one for low frequencies (LF). The core interferometer layout is based on a Michelson interferometer with Fabry-Perot cavities in the arms and recycling.

for example, they provide the possibility to steer the ET-HF beam around the suspension system of the ET-LF ITM, and they decouple the angle of incidence on the main beam splitter from the angle between the long interferometer arms [9,10].

In this paper we analyze different arm telescope designs with the target of achieving a 6 mm large beam waist at the main beam splitter. The constraint on the size of this waist (and thus the spot size on the beam splitter) is rationalized in Sec. II, where other constraints stemming from the design of the central interferometer and the arm cavities [1] are discussed as well. Regions of interest in our parameter searches, covered in Sec. III for ET-LF and in Sec. IV for ET-HF, are defined as regimes where the telescope configuration gives this 6 mm waist positioned at the beam splitter, while the SRC is stable. In Sec. V, we present an analysis on the sensitivity of the ET-LF telescope solution to each free parameter. Following on from this, a preliminary study quantifying the necessary active changes (for mode matching) to the telescope mirror curvatures in the presence of thermal lensing in the ITM is given. The results in this paper were obtained using beam parameter propagation [11] via the symbolic ABCD matrix capabilities of our open-source simulation software FINESSE 3 [12]. The methodology involved grid-based searches of the parameter space to find regions satisfying the aforementioned requirements. In this context, grid-based searches are defined as analyses of high-dimensional scans over any given free parameters. An independent verification of the results was performed using a new analytical framework for optimization of beam expansion telescopes in coupled cavities [13].

II. ARM CAVITY EIGENMODE AND TELESCOPE CONSTRAINTS

The maximal beam sizes on test masses are set via the tolerance on power lost through clipping at the mirror edge. The relation between the maximum beam size w_{max} to achieve a minimum clipping loss l_{clip} is given by

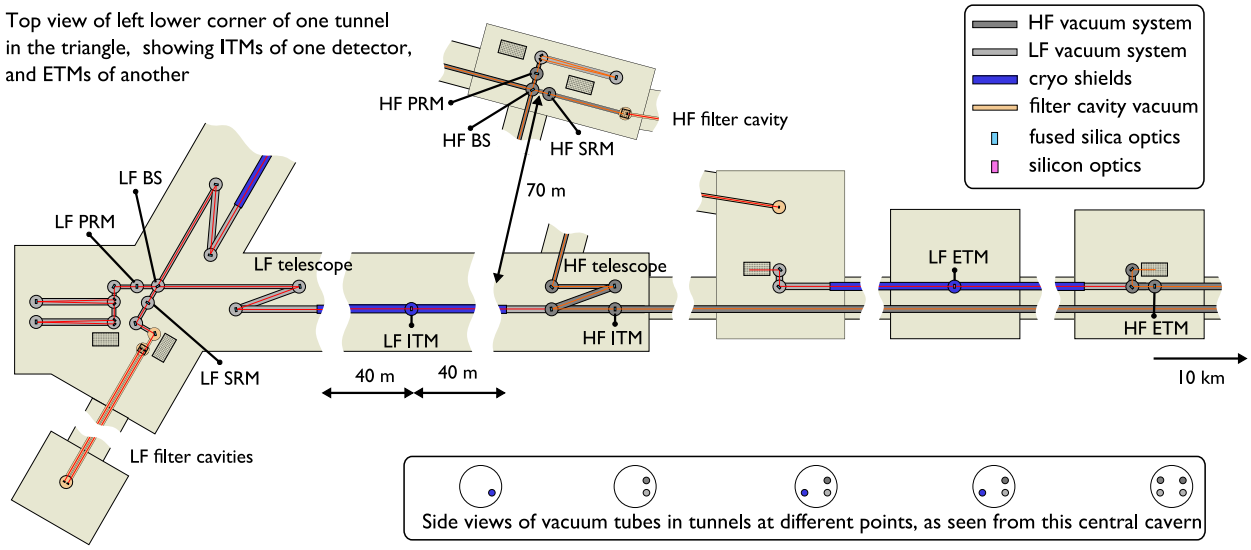

FIG. 2. This is a sketch of the lower left corner of the triangle, showing an example implementation of the optical layout, the vacuum system for the main optics and the corresponding cavern layout. In particular this shows the possible location of Z-shaped telescope systems for ET-LF and ET-HF detectors. In this example the telescopes have been placed to achieve an angle of incidence of 45° on the ET-HF beam splitter.

TABLE I. A summary of the key parameters of the ET-LF and ET-HF arm cavities. Note that we have assumed symmetric arm cavities for simplicity here.

	ET-HF	ET-LF
Wavelength (λ)	1064 nm	1550 nm
Cavity length (L)	10 km	10 km
Free spectral range ($\Delta\nu$)	15 kHz	15 kHz
ITM/ETM diameter (M_d)	62 cm	45 cm
ITM/ETM curvature (R_C)	5070 m	5580 m
Beam radius on ITM/ETM (w)	12.0 cm	9.0 cm
Beam radius at cavity waist (w_0)	1.42 cm	2.90 cm
Rayleigh range (z_R)	591 m	1702 m
Distance to waist from ITM (z_0)	5 km	5 km
Cavity stability factor (g)	0.95	0.63
Round-trip Gouy phase (ψ_{RT})	333°	285°
Mode separation frequency (δf)	1.1 kHz	3.1 kHz

$$w_{\max} = \sqrt{\frac{2}{\log(\frac{1}{l_{\mathrm{clip}}})}}R, \tag{1}$$

with R as the mirror radius [14]. The resulting beam sizes and corresponding mirror radii of curvature for ET-HF and ET-LF that satisfy the requirement of clipping loss of 1 ppm are listed in Table I. Note that the diameters of the mirrors shown in this table were taken directly from [1,15] but do not necessarily represent final design values. The arm cavity parameters shown in Table I are used to define the arm cavity model serving as the starting point of the beam propagation analyses in Sec. III.

A. Telescope parameter constraints

A simplified schematic of one beam-expander telescope is shown in Fig. 3. In order to reduce the impact of thermal noise on the sensitivity, ET-LF will make use of cryogenics to cool down the test masses to ~10 to 20 K. Cryoshields of around 40 m length will be used along the beam before and after the cryogenic mirrors [15], placing a lower limit on the distance between the telescope mirrors and the ITM, thus, commensurately setting a lower limit for the SRC length for ET-LF. In Secs. III B and III C this distance is kept fixed at the current design value of 52.5 m.

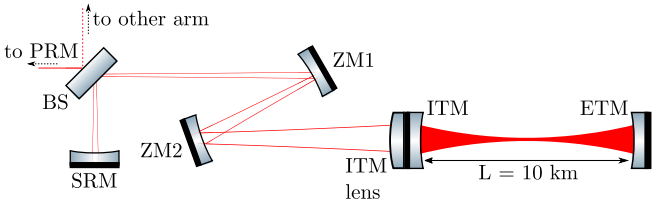

FIG. 3. Schematic of an ET arm telescope with a lens at the ITM. This type of configuration is used for the analyses in this section, where the Z mirrors are flat in Sec. III A while the lens has an infinite focal length in Sec. III B.

The picture is different for ET-HF, where a signal recycling cavity length of 100 m or less is preferred in order to improve the quantum-noise limited higher-frequency sensitivity [16]. ET-HF does not use cryogenics, so that the lower limit on the SRC length is given only by the minimum distance allowed between the vacuum tanks.

As stated in Sec. I, we targeted a waist size of 6 mm at the beam splitter. The final design for the size of the beam on the central beam splitter will be based on a trade-off study including the following considerations. In Advanced LIGO the main beam splitter sits between the telescopes and the arm cavities [6]—resulting in a spot size on the central beam splitter comparable to the beam size on the ITMs and thus requiring a large beam splitter to avoid clipping losses. In contrast, in this work, we propose placing the telescopes between the beam splitter and the arms, to allow use of a smaller beam splitter, an idea briefly discussed in [17]. Assuming a beam splitter radius of 15 cm and 60° intersection angle of two incident beams, sub-part-per-million clipping losses are achieved with beam sizes smaller than ~10 mm, setting an upper bound on the acceptable beam size at the beam splitter.

Similarly to GEO600 [18], ET-HF will operate with ~kilowatt levels of power on the central beam splitter [15]. As such, this circulating power will induce thermal lensing in the beam splitter substrate, as is the case for GEO600 [19]. This thermal lensing causes an undesirable excitation of higher-order modes and reduces the interferometric visibility. The strength of this lensing is related to the beam intensity and thus reduced with larger beams at the central beam splitter. For consistency between both solutions, a waist size of 6 mm at the central beam splitter was targeted for both ET-LF and ET-HF. It is important to note, however, that, in the case of ET-HF, this may contribute undesirably to scattering into higher-order modes. The strength of this effect will require further studies.

Note that although the targeted beam size on the beam splitter is 15–20 times smaller than that on the test masses of ET-LF and ET-HF, respectively, the thermal noise contribution from the main beam splitter is still much smaller than that from arm cavity mirrors, taking into account the arm cavity finesse, at around 900, and the fact that the beam splitter will have fewer coating layers and a smaller substrate volume.

III. ET-LF ARM TELESCOPE DESIGN

In this section we analyze potential arm telescope configurations focusing on achieving a stable SRC while keeping a waist size of $w_0 \sim 6$ mm near to the beam splitter. The analyses in this section are performed for ET-LF. In this and the following sections we will describe beam-expander telescopes with curved mirrors with a non-normal angle of incidence. With the commonly used spherical mirrors, such telescopes would suffer from astigmatism which would reduce the mode matching in the

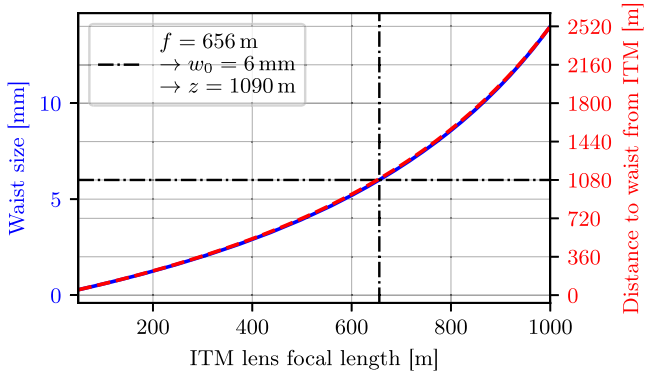

FIG. 4. The waist size (blue line) and distance to waist from ITM (red line) of a beam matched to the arm cavity for different ITM lens focal lengths. Highlighted on this plot is the focal length value which corresponds to our targeted waist size. Note that even with some flexibility on the waist size of a few millimeters, the required distance from the ITM to the waist is still on the order of at least 0.5 km.

interferometer. Note that the following computations assume spherical mirrors with small angles of incidence and negligible astigmatism. The schematic layout shown in Fig. 2 however implies relatively large angles of incidence, requiring nonspherical mirrors. If the final optical design will include significant angles of incidence, our results provide a good starting point for designing the required nonspherical surfaces, based on the desired beam parameters along the optical path.

A. Flat Z mirrors

The simplest beam-expander configuration possible is one based on a lens at the ITM while keeping the Z mirrors flat (i.e., they are just steering mirrors). Using our target waist size, we can deduce an ITM lens focal length value for this setup, which is shown in Fig. 4. Also displayed in that figure are the distances to the beam waist from the ITM. This figure demonstrates that a distance of ∼1 km is necessary for maintaining a waist, of the appropriate size, at (or near to) the beam splitter. Given the impracticality of this distance (implying a comparable SRC length), we can reject this type of configuration.

B. Curved telescope mirrors, and no lens at ITM

Allowing the mirrors in the Z configuration to have some curvature gives another type of beam-expander configuration which can be explored for feasibility. Based on the results in the single-lens case we expect ZM2 to have a positive radius of curvature (ROC) for converging the beam rapidly and ZM1 to have a negative ROC in order to achieve a small beam size on the beam splitter over a short distance.

Another criterion comes from the stability of the SRC. The setup has a significant number of free degrees of freedom, i.e., ROCs of ZM1 and ZM2, the telescope distance (the distance between ZM1 and ZM2) and other free spaces in the SRC, which determine the round-trip Gouy phase. But the basic behavior of this system can be understood intuitively when combining a basic understanding of beam propagation and our simulation results. Firstly, the accumulated Gouy phase contribution from ITM to ZM2 can be ignored, since this distance is much smaller than the Rayleigh range of the beam from the arm cavities which is ∼1.7 km as shown in Table I and the Gouy phase is calculated as

$$\psi = \arctan\left(\frac{z}{z_R}\right). \tag{2}$$

Secondly, the main Gouy phase contribution comes from the distance from SRM to the telescope, because the Gouy phase changes faster near to the beam waist position; see Eq. (2). For our analyses, a very short distance from the waist to the SRM of 10 m is assumed. Finally, a minimal distance ∼100 m between the beam-expander mirrors helps to reduce the overall SRC length to ∼250 m while retaining a 6 mm beam waist.

The results shown in Fig. 5 were obtained after a wide parameter space search. This figure shows that a stable SRC is possible; however, a relatively long SRC is required —on the order of 250 m on average—while the ROC of ZM1 is small relative to the ZM2 ROC. We can trade off the achievable SRC length and the required curvature of ZM1; i.e., a shorter SRC can be achieved by reducing the radius of curvature of this mirror—this ultimately comes down to a design choice, based on other design parameters outside the scope of this work.

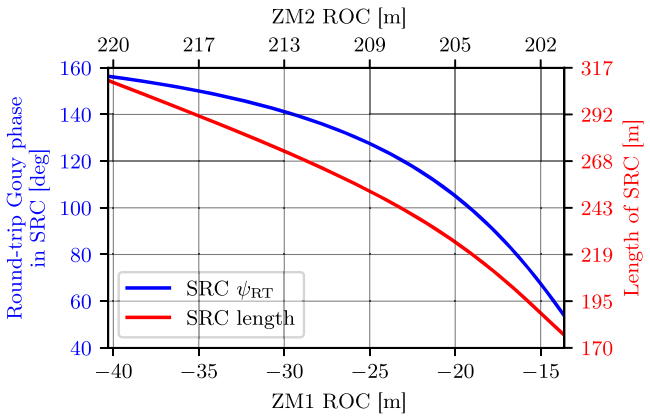

FIG. 5. ZM1 and ZM2 ROC combinations yielding a 6 mm waist size where the position of this waist is less than 150 m from ZM1. The blue trace shows the round-trip Gouy phase ψ_{RT} in the SRC. All the values in this trace satisfy the condition $20° \leq \psi_{\mathrm{RT}} \leq 160°$ so that every solution shown in this figure represents a stable SRC. The red trace gives the corresponding length of the SRC for each of the ROC combinations.

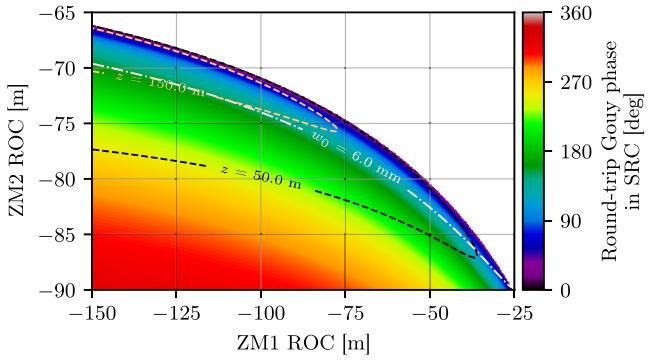

FIG. 6. SRC round-trip Gouy phase for an ITM lens of focal length $f = 75$ m and a distance between the Z mirrors of 50 m. Note that the solutions now require the curvatures of ZM1 and ZM2 to both be negative—this is because the ITM lens, of the focal length used here, is responsible for focusing the beam to a waist from the arm cavity. ZM1 collimates the beam going toward the beam splitter, while ZM2 acts as a "beam expander" to prevent the beam (as propagated from the arm cavity) from focusing down to a waist too quickly.

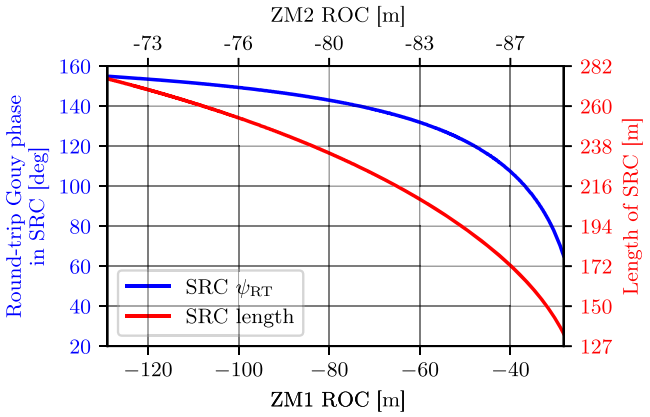

FIG. 7. The key take-away from this plot is that by introducing a lens, shorter SRC lengths can be obtained along with the option of less demanding (i.e., larger) ZM1 ROCs. Taking ZM1 ROC = −40 m as an example data point, we see from this plot that this corresponds to an SRC length of approximately 170 m and a round-trip Gouy phase of approximately 110°. Compare this to the same ZM1 ROC value on Fig. 5 which gives around 310 m and 155° for these quantities, respectively.

C. Curved telescope mirrors with a lens at the ITM

The previous solutions, shown in Fig. 5, lead to a relatively long SRC, > 100 m. In this section we will investigate how adding a lens at the ITM can be used to reduce the length of the SRC and relax the requirements on the radius of curvature of ZM1.

We produced a set of animated plots of the round-trip Gouy phase to gain an intuition of how the solution regions evolve. Similarly to Sec. III B, the content shown here is based on these wide parameter searches and thus only shows the conclusions. We find short focal lengths ($f \lessapprox 100$ m) that result in a real waist beyond the ZM1 optic give solutions satisfying our requirements. A focal length of $f = 75$ m was chosen for a more in-depth analysis. Note that any focal length comparable to this value will result in similar telescope behavior but with slightly different solutions for the ZM1 and ZM2 curvatures and distances to the waist.

Using this focal length, and a distance between the Z mirrors of 50 m, Fig. 6 was produced—giving the SRC round-trip Gouy phase over the ZM ROCs, with contours for the 6 mm waist size and distances to the waist (from ZM1) of 50 and 150 m overlaid on the plot. These contours, along with the color map, frame the region which provides potential configurations for achieving a stable SRC of a suitable length. It is immediately apparent from this figure that the range of possible ZM1 curvatures which give solutions is much larger than for the configuration with no lens at the ITM. Here the lens takes the role of focusing the beam such that both ZM1 and ZM2 have negative ROCs and act together to collimate the beam from the arm cavity. By inspecting Fig. 6 we find that this solution region

TABLE II. Parameters of the telescopes chosen using Fig. 7, with values for the beam size and accumulated Gouy phase associated with these given at each optic in the configuration. Note that the computed values have been given to 2 significant figures to avoid unnecessary precision at this stage. Where appropriate, values for LF and HF have been given separately. See Fig. 8 for a visual representation of these data for ET-LF. The focal length of the ITM lens, in both cases, is 75 m.

Optic		SRM	BS	ZM1	ZM2		
ROC [m]	LF	−9410	inf	−50	−82.5		
	HF	−630			−63.2		
Beam radius [mm]	LF	6.1	6.2	8.9	30		
	HF	6.3	6.4	8.3	38		
Space		SRM-BS	BS-ZM1	ZM1-ZM2	ZM2-1TM		
Length [m]	LF	10	70	50	52.5		
	HF			80			
Gouy phase [deg]	LF	7.5	39	5.3	0.6	Total accumulated	52
	HF	4.8	26	4.9	0.2	Gouy phase [deg]	36

approximately corresponds to ZM1 ROC $\in [-130\text{ m}, -30\text{ m}]$ and ZM2 ROC $\in [-70\text{ m}, -90\text{ m}]$. This region is shown in Fig. 7.

We can use Fig. 7 to pick a reference solution for the telescope parameters. One such solution set is given in Table II, where the curvature combinations were chosen such that a relatively short SRC is obtained (important for ET-HF; see Sec. II A) while the edges of the solution range are avoided (i.e., avoiding a near-unstable SRC). The resulting g factor of the signal recycling cavity for this solution set is $g \sim 0.37$. In addition, this solution yields $> 99.9\%$ mode matching between the SRC and arm cavity. A discussion of the ET-HF results, also stated in Table II, is given in Sec. IV.

IV. ET-HF ARM TELESCOPE DESIGN

The ET-LF solution given in Table II was used as a starting point for a similar analysis on the ET-HF arm telescope. The results are then given in the same table, denoted with HF to distinguish the values from LF where appropriate. The larger beam size (impinging on the arm cavity mirrors; see Table I), and shorter wavelength of ET-HF, result in the requirement for a longer telescope length when considering the same waist size target of 6 mm. This increased length requirement can potentially be relaxed by decreasing this waist size target; however, the required trade-off study is beyond the scope of this paper. The solution given for ET-HF in Table II is optimized given this waist (and stable SRC) requirement. Note, also, that the ET-HF solution uses the same ITM lens focal length ($f = 75$ m) as the ET-LF solution found in Sec. III C. The resulting g factor of the signal recycling cavity for this solution set is $g \sim 0.65$. The solution stated also yields $> 99.9\%$ mode matching between the SRC and arm cavity.

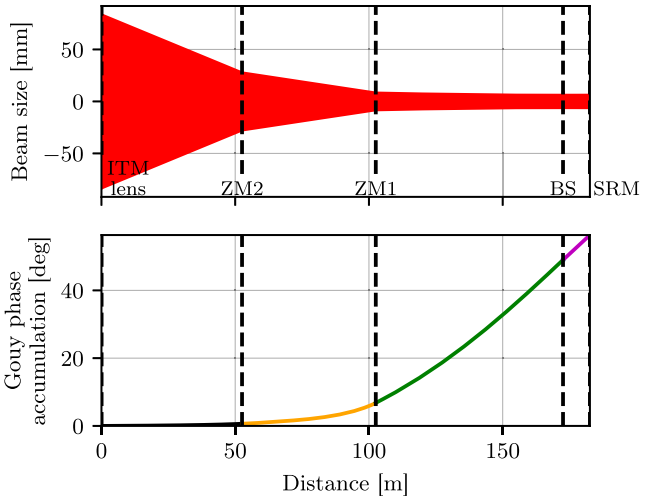

FIG. 8. The ET-LF telescope design from the arm cavity to the SRM is shown, where the beam size and accumulated Gouy phase are plotted over the distance propagated through the SRC. Note that, while the beam sizes and telescope length differ slightly for ET-HF, the beam remains collimated in the ZM1 to SRM path; this is an important consideration for Fig. 9.

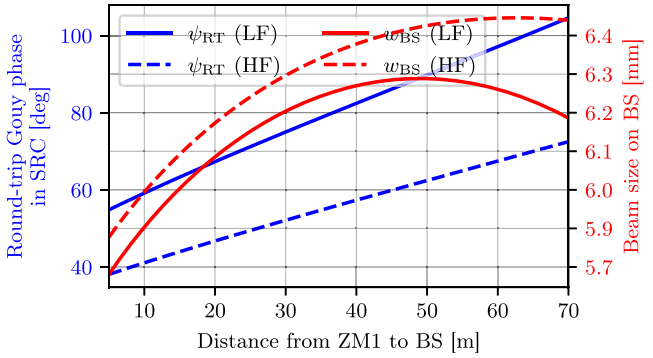

FIG. 9. The accumulated round-trip Gouy phase in the SRC and radius of the beam impinging on BS for both ET-LF and ET-HF where the distance between the ZM1 and BS is decreased from its nominal value given in Table II. All other telescope parameters are kept constant.

Given that both the solutions for ET-LF and ET-HF result in a beam that is roughly collimated between ZM1 and the SRM (see Fig. 8), we can alter the distance between BS and ZM1 without affecting the beam size on the beam splitter by much more than a few hundred microns. This is demonstrated in Fig. 9. Even by reducing this distance significantly, e.g., to 10 m, a stable SRC can still be obtained for both ET-LF and ET-HF (with $\psi_{RT} \approx 60$ and $\psi_{RT} \approx 40°$, respectively), where the beam size on the beam splitter would then be around 5.7 and 5.9 mm for ET-LF and ET-HF, respectively. Of particular importance to ET-HF, this could allow for a nominal reduction in the SRC length from 210 to around 150 m while keeping the other telescope parameters, shown in Table II, constant.

V. PARAMETER SENSITIVITY AND MODE MATCHING

Taking the results found in the end of Sec. III C as our baseline configuration, we can determine the critical parameters of, for example, our ET-HF telescope design. These can be determined by deviating the key free parameters of the system to observe the effect on the SRC waist size, round-trip Gouy phase and mode matching to the arm cavity. Figure 10 displays the results of such an analysis, where the left plots give the aforementioned target parameters as a function of the distances between the optics while the right plots are based on deviations in the radii of curvature of the Z mirrors and the focal length of the ITM lens.

The mode-matching quantity shown in Fig. 10 is defined by the "overlap" ($\mathcal{O}$) figure of merit [20],

$$\mathcal{O} = \frac{4|\mathrm{Im}\{q_1\}\mathrm{Im}\{q_2\}|}{|q_1^* - q_2|^2}, \tag{3}$$

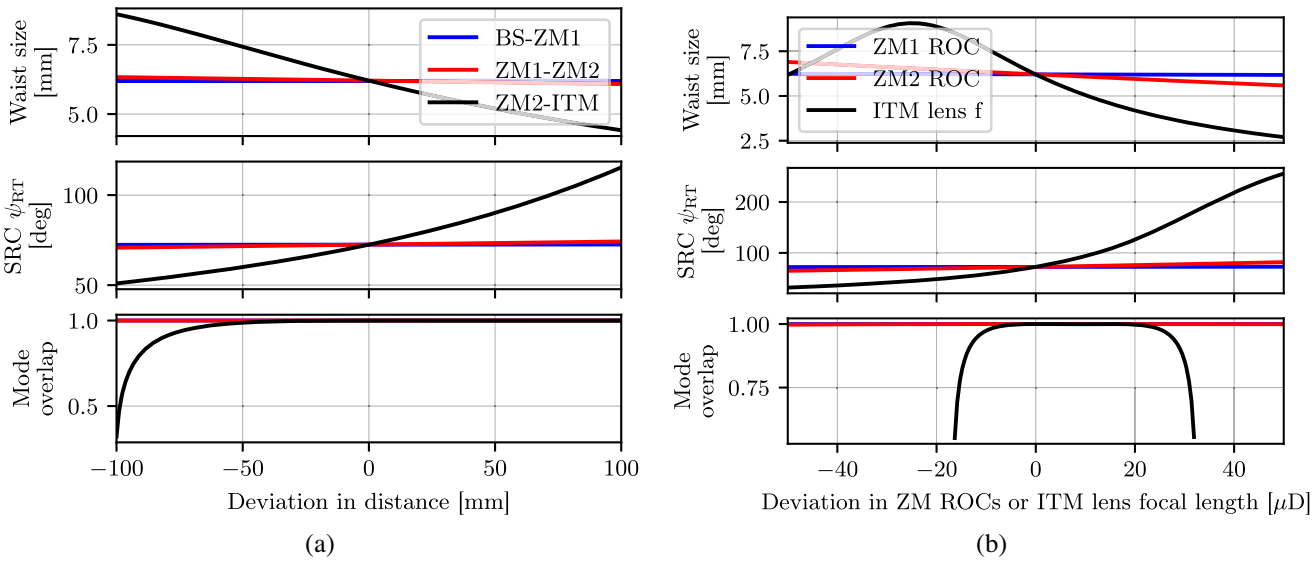

FIG. 10. SRC waist size, round-trip Gouy phase and mode overlap with the arm cavity as functions of the key distances between optics (a) and the curvatures of the telescope optics (b). Each deviation is given in relative terms where a value of zero corresponds to the (ET-HF) baseline value given in Table II. From (a) we can see that the distance between the ITM and ZM2 is the most critical length. While, in (b), we find that the focal length of the ITM lens is the critical parameter in terms of the optic geometries. Note that the mode-matching values in the lower subplot were computed via Eq. (3).

where q_1 and q_2 are the beam parameters being compared. In this case q_1 represents the eigenmode of the SRC propagated to the arm cavity and q_2 is the arm cavity mode itself. This quantity returns values $\mathcal{O} \in [0, 1]$, where unity indicates a full mode match between the two beam parameters and zero gives complete mode mismatch.

From Fig. 10 we can deduce, in terms of the optic geometries, that this telescope configuration is most sensitive to the focal length of the lens at the ITM. Thus the next step of this analysis will focus solely on the ITM lens focal length changes as a result of thermal aberrations in the beam. Thermal lensing is investigated, in particular, due to it, potentially, being responsible for the largest effective changes to the ITM lens focal length—as shown at the end of the next section.

A. Mode matching in the presence of thermal lensing

Surface deformation and refractive index differentials, caused by temperature distributions in the mirror substrates, lead to thermal aberrations (lensing) in the beam in ground-based gravitational-wave detectors [21]. This thermal lensing results in mode mismatches between the arm and recycling cavities. In terms of the optics present in our configuration, the thermal lensing acts to modify the effective focal length of the ITM lens, thereby altering the geometry of the beam in the signal recycling cavity (see the solid traces in Fig. 10 for this effect in a broad sense). To minimize these distortions, adaptive optics are required [22,23]. This is one of the tasks which could be performed by the arm telescopes of the ET detectors; thus, in this section we will quantify the required deviations to the telescope mirror curvatures, for recovering mode matching to the arm cavities, in the presence of varied thermal lens focal lengths. In this case the ET-HF telescope (plus arm cavity) configuration is used, as this detector is designed to operate at high power [1,15] where thermal lensing will be more prevalent.

Figure 11 quantifies the necessary modifications to the radii of curvature of ZM1 and ZM2 in order to recover $> 99.9\%$ mode matching of the SRC to the arm cavity, for an assumed range of thermal lens focal lengths of $f_{\mathrm{th}} \in [100\ \mathrm{km}, 15\ \mathrm{km}]$. Note that for a strong focal length

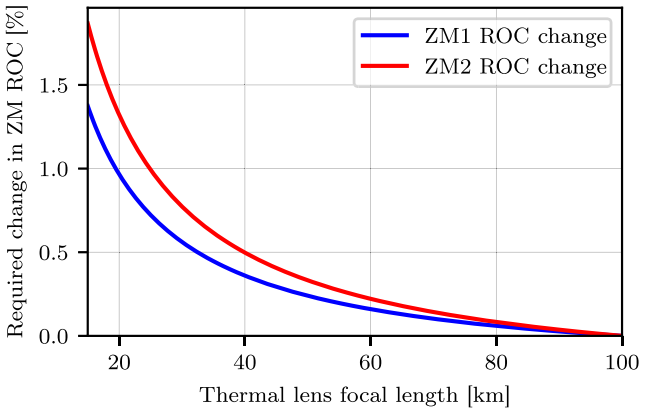

FIG. 11. Simultaneous changes in Z mirror ROCs required for recovering "complete" mode matching from the SRC to the arm cavity. At the extreme of $f_{\mathrm{th}} = 15$ km on this plot, the required deviation in the ROC of ZM1 is approximately 1.4% while for ZM2 it is 1.9%.

of 15 km from the thermal lens, the effective focal length of the ITM reduces to $f \approx 74.63$ m, i.e., a deviation of about 0.5% from the target value of 75 m noted in Sec. V. This focal length distortion results in a mode mismatch, between the arm cavity and signal recycling cavity, of approximately 20%. At this extreme thermal lens, the modifications to the Z mirror radii of curvature indicated by Fig. 11 reduce this mode mismatch to effectively 0%.

VI. CONCLUSION

In this paper we investigated arm telescope configurations, for both ET-LF and ET-HF, which are suitable for the optical layout in the ET 2020 design update [1]. These telescope configurations are motivated by smaller beams on the optics in the central part of the interferometer. The beam expanders also provide the ability to steer the ET-HF beam around the ET-LF ITM suspension systems, with the added benefits of decoupling the angle of incidence on the beam splitter from the beam axes in the interferometer arms. Our requirements for this telescope can be summarized as targeting a 6 mm waist size positioned at the main beam splitter while maintaining a stable SRC (quantified approximately as having a length of the same order as the Rayleigh range of the beam). Further details on these requirements were given in Sec. II A.

We demonstrated that it is possible to achieve a stable SRC, of a sensible length, with telescopes in the arms of both the ET-LF and ET-HF interferometers. Reducing the length of SRC, in accordance with [16], can be attained via the introduction of a lens at the ITM for prefocusing the beam from the arm cavity. Our baseline solutions for such a configuration are given in Table II. Further reductions to the length of the SRC, while changing the spot size on the beam splitter by only a few hundred microns, are possible via decreasing the distance from ZM1 to BS—see Fig. 9 for details.

Our baseline configuration for ET-HF was analyzed in Sec. V where we found that the focal length of the ITM lens is the critical parameter in terms of the sensitivity for mode matching and SRC stability. However, in Sec. V A, we found that effective changes in this focal length due to thermal lensing can be compensated with actuation on the curvatures of the telescope mirrors. In particular, we saw that the mode mismatch (of approximately 20%) due to a strong thermal lens, with $f_{\mathrm{th}} \sim 15$ km, can be fully corrected with changes of approximately 1.4% and 1.9% in the ROCs of ZM1 and ZM2, respectively.

The results presented here provide evidence for the feasibility of beam-expander telescopes in the interferometer arms of ET and provide essential input for trade-off studies of the optical layout. Further studies are required to study other aspects of this setup, in particular the effects of astigmatism in specific telescope implementations, and the possible negative impact on the contrast defect due to having the telescopes in a configuration that allows differential beam tuning.

ACKNOWLEDGEMENTS

We are grateful to Annalisa Allocca and Daniel Toyra for useful comments. This work has been supported by the Science and Technology Facilities Council (STFC). A. F. has been supported by a Royal Society Wolfson Fellowship which is jointly funded by the Royal Society and the Wolfson Foundation. This paper has been assigned LIGO Document No. LIGO-P2000417.

[1] ET Steering Committee Editorial Team, Einstein Telescope Design Report Update 2020 (Einstein Telescope Collaboration, 2020).

[2] M. Maggiore, C. V. D. Broeck, N. Bartolo, E. Belgacem, D. Bertacca, M. A. Bizouard, M. Branchesi, S. Clesse, S. Foffa, J. García-Bellido, S. Grimm, J. Harms, T. Hinderer, S. Matarrese, C. Palomba, M. Peloso, A. Ricciardone, and M. Sakellariadou, Science case for the Einstein telescope, J. Cosmol. Astropart. Phys. 03 (2020) 050.

[3] J. Aasi, B. P. Abbott, R. Abbott, T. Abbott, M. R. Abernathy, K. Ackley, C. Adams, T. Adams, P. Addesso, R. X. Adhikari, and LIGO Scientific Collaboration, Advanced LIGO, Classical Quantum Gravity **32**, 074001 (2015).

[4] F. Acernese, M. Agathos, K. Agatsuma, D. Aisa, N. Allemandou, A. Allocca, J. Amarni, P. Astone *et al.*, Advanced Virgo: A second-generation interferometric gravitational wave detector, Classical Quantum Gravity **32**, 024001 (2015).

[5] A. Buonanno and Y. Chen, Scaling law in signal recycled laser-interferometer gravitational-wave detectors, Phys. Rev. D **67**, 062002 (2003).

[6] M. A. Arain and G. Mueller, Design of the advanced LIGO recycling cavities, Opt. Express **16**, 10018 (2008).

[7] C. Buy, E. Genin, M. Barsuglia, R. Gouaty, and M. Tacca, Design of a high-magnification and low-aberration compact catadioptric telescope for the advanced virgo gravitational-wave interferometric detector, Classical Quantum Gravity **34**, 095011 (2017).

[8] T. Zhang, S. L. Danilishin, S. Steinlechner, B. W. Barr, A. S. Bell, P. Dupej, C. Gräf, J.-S. Hennig, E. A. Houston, S. H. Huttner, S. S. Leavey, D. Pascucci, B. Sorazu, A. Spencer, J. Wright, K. A. Strain, and S. Hild, Effects of static and dynamic higher-order optical modes in balanced homodyne readout for future gravitational waves detectors, Phys. Rev. D **95**, 062001 (2017).

[9] R. DeSalvo, Considerations on Michelson beam splitters for third generation gravitational wave observatories, https://dcc.ligo.org/LIGO-G1900927/public (2020).
[10] R. DeSalvo *et al.*, Beam expander telescopes for the Michelson beam splitters in third generation gravitational wave observatories (to be published).
[11] H. Kogelnik, On the propagation of gaussian beams of light through lenslike media including those with a loss or gain variation, Appl. Opt. **4**, 1562 (1965).
[12] D. Brown, S. Rowlinson, S. Leavey, P. Jones, and A. Freise, FINESSE 3, https://git.ligo.org/finesse/finesse3 (2020).
[13] A. Dmitriev *et al.*, Optimisation of beam expansion telescopes for third-generation gravitational wave detectors (to be published).
[14] C. Bond, D. Brown, A. Freise, and K. Strain, Interferometer techniques for gravitational-wave detection, Living Rev. Relativity **19**, (2017).
[15] The ET Science Team, Einstein Gravitational Wave Telescope Conceptual Design (European Commission, 2011).
[16] P. Jones, T. Zhang, H. Miao, and A. Freise, Implications of the quantum noise target for the einstein telescope infrastructure design, Phys. Rev. D **101**, 082002 (2020).
[17] M. Granata, M. Barsuglia, R. Flaminio, A. Freise, S. Hild, and J. Marque, Design of the advanced Virgo non-degenerate recycling cavities, J. Phys. Conf. Ser. **228**, 012016 (2010).
[18] H. Lck, C. Affeldt, J. Degallaix, A. Freise, H. Grote, M. Hewitson, S. Hild, J. Leong, M. Prijatelj, K. A. Strain, B. Willke, H. Wittel, and K. Danzmann, The upgrade of GEO 600, J. Phys. Conf. Ser. **228**, 012012 (2010).
[19] H. Wittel, C. Affeldt, A. Bisht, S. Doravari, H. Grote, J. Lough, H. Lück, E. Schreiber, K. A. Strain, and K. Danzmann, Matrix heater in the gravitational wave observatory geo 600, Opt. Express **26**, 22687 (2018).
[20] F. Bayer-Helms, Coupling coefficients of an incident wave and the modes of a spherical optical resonator in the case of mismatching and misalignment, Appl. Opt. **23**, 1369 (1984).
[21] H. Patrice and V. Jean-Yves, Analytical models of thermal aberrations in massive mirrors heated by high power laser beams, J. Phys. II (France) **51**, 1267 (1990).
[22] A. F. Brooks, B. Abbott, M. A. Arain, G. Ciani, A. Cole, G. Grabeel, E. Gustafson, C. Guido, M. Heintze, A. Heptonstall, M. Jacobson, W. Kim, E. King, A. Lynch, S. O'Connor, D. Ottaway, K. Mailand, G. Mueller, J. Munch, V. Sannibale, Z. Shao, M. Smith, P. Veitch, T. Vo, C. Vorvick, and P. Willems, Overview of advanced LIGO adaptive optics, Appl. Opt. **55**, 8256 (2016).
[23] A. Rocchi, E. Coccia, V. Fafone, V. Malvezzi, Y. Minenkov, and L. Sperandio, Thermal effects and their compensation in advanced virgo, J. Phys. Conf. Ser. **363**, 012016 (2012).